Journal Pre-proofs

Tumor-targeted delivery of Silibinin and IPI-549 synergistically inhibit breast cancer by remodeling the microenvironment

Min Jiang, Kaiyong He, Tong Qiu, Jiahui Sun, Qi Liu, Xueqiong Zhang, Hua Zheng

PII: S0378-5173(20)30223-4
DOI: https://doi.org/10.1016/j.ijpharm.2020.119239
Reference: IJP 119239

To appear in: *International Journal of Pharmaceutics*

Received Date: 18 December 2019
Revised Date: 6 March 2020
Accepted Date: 15 March 2020

Please cite this article as: M. Jiang, K. He, T. Qiu, J. Sun, Q. Liu, X. Zhang, H. Zheng, Tumor-targeted delivery of Silibinin and IPI-549 synergistically inhibit breast cancer by remodeling the microenvironment, *International Journal of Pharmaceutics* (2020), doi: https://doi.org/10.1016/j.ijpharm.2020.119239

Tumor-targeted delivery of Silibinin and IPI-549 synergistically inhibit breast cancer by remodeling the microenvironment

Min Jiang[a], Kaiyong He[b], Tong Qiu[a], Jiahui Sun[a], Qi Liu[c], Xueqiong Zhang[a,*], Hua Zheng[a,*]

[a]School of Chemistry, Chemical Engineering and Life Sciences, Wuhan University of Technology, Wuhan 430070, China
[b]Hubei Institute for drug control, Wuhan 430070, China
[c]Department of Dermatology, Johns Hopkins University School of Medicine, Baltimore, MD, 21231, USA

[*]Corresponding author: Xueqiong Zhang, Tel.: +86 138 8612 3736
E-mail address: zxqiong0204@163.com
Corresponding author: Hua Zheng, Tel.: +86 138 7117 4722
E-mail address: zhenghua.whut@126.com

ABSTRACT

We induced changes in the tumor microenvironment (TME) through the synergistic actions of two drugs used in breast cancer therapy. The anti-fibrotic drug silibinin (SLB) targets tumor-associated fibroblasts and exerts immune-mediated anti-cancer effects. IPI-549, an efficient and highly selective phosphoinositide-3-kinase-gamma (PI3Kγ) inhibitor, was applied to alter the balance of immunosuppressive cells by inhibiting PI3Kγ molecules; it also promotes anti-tumor immunity. We developed nanoparticle formulations to encapsulate both drugs into the targeting carrier aminoethyl anisamide-polyethylene glycol-polycaprolactone (AEAA-PEG-PCL) respectively. The drugs were intravenously delivered in mice and resulted in an increase in anti-tumor efficacy and apoptotic tumor tissue compared with either IPI-549 or SLB alone in 4T1 breast cancer cell-derived tumors. Furthermore, a significant reduction in regulatory T (Treg) cells and myeloid suppressor cells (MDSCs) was observed. A normalized TME structure was also observed, including angiogenesis suppression, antifibrotic effects and the inhibition of collagen formation in the tumor tissue, significantly enhancing the anti-tumor effects. In summary, this combination strategy may offer an alternative treatment for breast cancer.

KEY WORDS: Tumor microenvironment; Phosphoinositide-3-kinase-gamma; Combination; Therapy; AEAA-PEG-PCL; Breast cancer;

1. Introduction

In recent years, the prevalence of breast cancer has shown a clear increasing trend (Siegel et al., 2019). There is increasing evidence that breast cancer progression depends to a large extent on the tumor microenvironment (TME) (Francoa et al., 2019; Houthuijzen and Jonkers, 2018), which includes a variety of immune cells, such as tumor-associated fibroblasts (TAFs), tumor-associated macrophages (TAMs), regulatory T (Treg) cells and myeloid suppressor cells (MDSCs). MDSCs are a group of heterogeneous immune cell populations, including myeloid cell precursors, immature granulocytes, monocytes, and dendritic cells and are also known as immature immunity due to their immunosuppressive function (Lei and Zhou, 2014; Vlachou et al., 2012). Treg cells are essential for maintaining autoimmune homeostasis and are an important factor in inhibiting the formation of tumor-suppressive microenvironments (Gao et al., 2014). In view of the powerful functions of Treg cells, changes in Treg cells in tumor tissues are also an important issue. Both Treg cells and MDSCs correlate with tumor occurrence, development and prognosis, and their overexpression in various malignant tumor tissues has been shown (Wallecha et al., 2013; Weed et al., 2015). A study found that breast tumor growth in mice induces the accumulation of TAMs (Franklin et al., 2014), which in turn increases TAM concentration in breast tumor-bearing mice. Studies have shown that a highly selective phosphoinositide-3-kinase-gamma (PI3Kγ) inhibitor, IPI-549, can significantly improve the response of tumors with high TAM concentrations to immunological checkpoint blocking therapy (Janku, 2017). In addition, silibinin (SLB) is an anti-fibrotic drug that significantly inhibits TAFs in the tumor microenvironment (Ko et al., 2017). As the most abundant stromal cell in TME, TAFs play a key role in immunotherapy (He et al., 2017). We targeted TAFs with the anti-fibrotic drug, SLB, which when combined with IPI-549, may be a novel therapeutic approach for breast cancer through adjusting these immunosuppressive cells in the TME.

A related study (Nature, 2016) indicated that blocking PI3Kγ molecule can effectively reduce the activity of pretumor macrophages and enhance the function of anti-tumor macrophages to alter the balance of immunosuppressive cells and promote anti-tumor immunity (De Henau et al., 2016; Pathria et al., 2019). In addition, the effective inhibition and selectivity of IPI-549 is more than 100 times that of other lipids and protein kinases and 58-282 times that of other PI3K subtypes, with a biochemical IC50 of 16 nM (Evans et al., 2016). In a variety of tumor models, IPI-549 increased anti-tumor immunity by reducing MDSCs and increasing Treg cells, significantly inhibiting the growth of transplanted tumors and improving the sensitivity of certain tumors to existing anti-cancer drugs by synergistically enhancing the ability of existing cancer immunotherapy to eradicate tumors (Yu et al., 2019).

SLB is an anti-tumor agent, which mechanism is through anti-oxidation, anti-lipid peroxidation, anti-fibrosis, cell membrane stability, immunity, and regulation (Hammam and El, 2012). Meanwhile, many reports have demonstrated that the anti-fibrosis is associated with a reduction of alpha-smooth muscle (α-SMA)-positive cells and procollagen mRNA (Polachi et al., 2016). In recent years, SLB

has been found to have anti-tumor activity and has a good inhibitory effect on breast cancer (Hossainzadeh et al., 2019).

Unfortunately, SLB and IPI-549 have poor water solubility and low selectivity, and few studies have targeted nanoformulations that specifically deliver SLB and IPI-549 to tumor cells.

We report the use of the nanosedimentation method to effectively encapsulate IPI-549 and SLB into the targeted polymer carrier aminoethyl anisamide-polyethylene glycol-polycaprolactone (AEAA-PEG-PCL) to prepare nanoparticles, and we evaluated the toxicity of the preparation on breast tumors in vivo and in vitro. Ligand installed on the surface of nanocarriers can inhance nanoparticles targeting abilities (Lin et al., 2018; Mi et al., 2019). The sigma receptor is a membrane protein, and express on many tumor cells (van Waarde et al., 2015). Recent studies have found that sigma receptors are highly expressed on the surface of cancer cells and TAFs, and AEAA is a ligand for sigma receptors (Hou et al., 2018; Liu et al., 2019). If the sigma receptor ligand AEAA is attached to the surface of the drug delivery system, the drug can be specifically delivered to the critical immune suppressive cells in the tumor (Huo et al., 2017; Zhao et al., 2015). Therefore, the biodegradable amphiphilic polymer PEG-PCL was modified with AEAA, which allows the modified nanoparticles (NPs) to release drugs in tumor tissues (Zhang et al., 2019). We hypothesized that the two nanoparticles would actively target breast tumors and remodel the TME synergistically to enhance anticancer efficacy through immunotherapy.

2. Methods

2.1. Materials

IPI-549 was purchased from Chemietek (Indianapolis, IN, USA). Silibinin (SLB) was purchased from Chengdu Mansite Biotechnology Co., Ltd. (China). Tert-Butoxycarbonyl-Amino-Polyethylene Glycol-Amino-(Boc-NH-PEG2000-NH_2) was purchased from Shanghai Ponsure Biotechnology Co., Ltd. (China). Polycaprolactone-carboxy (PCL5000-COOH) was purchased from Xi'an Ruixi Biological Technology Co., Ltd. (China). p-Methoxybenzoyl chloride, 2-bromoethylamine hydrobromide, N,N-diisopropylethylamine (DIPEA), trifluoroacetic acid (TFA), dichloromethane (DCM) and N,N-diisopropylcarbodiimide (DIC) were purchased from Aladdin Industrial Inc. (China). Roswell Park Memorial Institute 1640 (RPMI-1640), 0.25% trypsin and double antibody were obtained from HyClone and Thermo Fisher Scientific. Fetal bovine serum (FBS), cell counting kit-8 (CCK-8), 4,6-diamidino-2-phenylindole (DAPI), and 4% paraformaldehyde fixative were obtained from Beyotime Institute of Biotechnology (Shanghai, China). Deionized water was produced by a water purifier (Aquapro, Chongqing, China). Mouse breast cancer cells (4T1 cells) were purchased from the China Center for Type Culture Collection; Female balb/c mice (6-7 weeks old) were provided by Wuhan Greenson Island Biotechnology Co., Ltd. (China) and raised at the specific pathogen-free (SPF) Animal Center of Hubei Food and Drug Administration. The experimental unit used the license number

[SYXK (E) 2019-0009], the unit license number [SCKY (E) 2015-0018]. The environment is sterilized by ultraviolet light on a regular basis, maintaining a constant temperature of approximately 20 °C, a relative humidity of approximately 50%, a photoperiod of 12 h each day, and feeding the mice with a basic diet. All operations are performed in an aseptic workstation in an SPF environment and in accordance with Chinese law. All drugs and reagents were obtained from commercial corporations without further processing.

2.2. Synthesis of AEAA-PEG-PCL

A total of 341 mg of p-methoxybenzoyl chloride (2 mmol), 410 mg of 2-bromoethylamine hydrobromide (2 mmol), and 180 μL of DIPEA were dissolved in 5 mL of acetonitrile and reacted at 40°C overnight; 400 mg of NH_2-PEG-NH-Boc (Mw = 2000, 0.2 mmol) was added, and the samples were stirred for 24 h. After the reaction, the mixture was added to 30 mL of ethyl ether and centrifuged for 10 min at 10,000 RCF; then, the tubes were stored at -20 °C for 2 h, centrifuged at 8000 RPM and -4 °C for 5 min to compact the precipitate. Then, the waste ether was removed, and the samples were washed with ether twice to give final purified product (240.8 mg, yield: 60.2%).

The precipitate (240.8 mg AEAA-PEG-NH_2-Boc) was resuspended in 4.5 mL of TFA /DCM (1/2 by vol). After stirring at RT for 2 h, the solvent was removed in a vacuum. The precipitate was redissolved in 5 mL of DCM and precipitated into the ether. Then, the sample was centrifuged at 10,000 RCF and -4°C for 15 min to compact the precipitate. After completion, the waste ether was removed, and the sample was washed with ether twice. The waste ether was removed, and the precipitate was dried under nitrogen gas for 2 - 4 h. The dry AEAA-PEG-NH_2·TFA (233.6 mg, yield: 97%) was transferred to a 20-mL vial for the next reaction.

A total of 233.6 mg of AEAA-PEG-NH_2·TFA, 600 mg of PCL-COOH (Mw = 5 kDa, 0.12 mmol), 132 μL of DIPEA, and 250 μL of DIC were dissolved in 6 mL of DCM. After stirring at RT for 48 h, the AEAA-PEG-PCL in DCM was dropwise added into methanol. The sample was centrifuged at 10,000 RCF and -0 °C for 15 min to compact the precipitate. The waste methanol was removed, and the sample was washed with methanol twice. Then, the waste methanol was removed, and the precipitate was dried under nitrogen for 1 h to give AEAA-PEG-PCL (560.2 mg, yield: 67.2%). The specific synthetic route is shown in Scheme 2. The chemical structures of the synthesized samples above were confirmed by a Fourier infrared spectrometer (Avator360, Nicolet, MA, USA) and Nuclear magnetic resonance instrument (Varian, USA).

2.3. Embedding silibinin and IPI-549 into AEAA-PEG-PCL using solvent displacement

A total of 75 mg AEAA-PEG-PCL polymer targeting vector and 5 mg of IPI-549/SLB were accurately weighed and placed in 500 μL of anhydrous acetone. After complete dissolution, the carrier was mixed with IPI-549 and SLB. The mixed solution was slowly dropped continuously into distilled water with stirring

and stirred at 40 °C for 7 h. After completion, the reaction solution was removed and centrifuged at 8000 RPM for 15 min, and the precipitate was removed. The supernatant was finally passed through a 0.45-μm filter membrane and lyophilized to obtain AEAA-PEG-PCL-IPI-549 and AEAA-PEG-PCL-SLB NPs lyophilized powders.

2.4. Characterization of nanoparticles

The particle size distribution and polydispersity index (PDI) of the two groups of nanoparticles were measured by dynamic light scattering (DLS) instrument (Malvern, UK).

The morphologies of the nanoparticles were obtained using a transmission electron microscope (TEM) (Tecnai G220 S-TWIN, FEI, USA) at an acceleration voltage of 100 kV. Briefly, the freshly prepared nanoparticle solution (1 mg/mL) was dropped on a copper mesh and allowed to dry naturally.

Determination of critical micelle concentration (CMC) of AEAA-PEG-PCL NPs by pyrene fluorescence probe method with a fluorescence spectrophotometer (F-7000, Hitachi High, Japan).

IPI-549 and SLB nanoparticles lyophilized powders were dissolved in deionized water. The content of the IP-549 and SLB was determined by ultraviolet spectrophotometry (UV 1101, Techcomp, China) at 267 and 288 nm. The encapsulation rate (EE) and drug-loading capacity (DLC) of the IPI-549 and SLB NPs were calculated according to the following formulas:

$$\mathrm{EE} = \frac{\text{Amounts of drug in NPs}}{\text{Total amount of drug}} \times 100\%$$

$$\mathrm{DL} = \frac{\text{Amounts of drug in NPs}}{\text{Total weight of NPs}} \times 100\%$$

2.5. In vitro SLB and IPI-549 release from NPs

The in vitro release behaviors of IPI-549 and SLB from nanoparticles were investigated by the dynamic dialysis method in PBS (pH 7.4). First, 5 mL of freshly prepared nanoparticle solution was taken, packaged in a dialysis bag, and placed in a centrifuge tube containing 45 mL of PBS (pH 7.4). A constant temperature of 37 °C was maintained, and the sample oscillated for 72 h at a speed of 100 rev/min. Subsequently, 3 mL of the drug release medium was withdrawn at the set time to be measured by UV. The total volume of the release medium of each group was maintained by supplementation; the cumulative release of IPI-549 and SLB was determined using the following formula, and the release curve was generated.

$$Q\% = \frac{45C_{\mathrm{n}} + 3\sum_{i=1} C_i}{m_{drug}} \times 100\%$$

where C_i and C_n refer to the mass concentration of drug in the release medium at the i and n moment, respectively.

2.6. Cell toxicity and in vitro synergistic effects

To verify the anticancer efficiency of the coadministered nanoparticles prepared herein, first, in vitro cell-level simulation experiments were performed, and the cytotoxicity of each component was determined using the CCK-8 method. First, 4T1 cells were propagated to a complete culture solution of medium/FBS/double antibody (89/10/1 by vol) and kept in an incubator at 5% CO_2 and at 37 °C. Then, 4T1 cells grown to log phase were seeded at a density of 8,000 cells/well in 96-well plates, and the incubation time was recorded. After the cells were incubated for 24 h and exhibited good growth, the original culture solution in each well was discarded. Afterwards, the six groups of 100 μL of different concentrations samples of PEG-PCL, AEAA-PEG-PCL, SLB, SLB NPs, IPI-549, IPI-549 NPs, SLB+IPI-549, and SLB+IPI-549 NPs were plated into 96-well plates, and the cells were further incubated for 24 and 48 h. Each sample was repeated six times, and untreated cells acted as a control. The culture solution in each well was replaced by 100 μL of CCK-8 reagent (90%) in the dark. The cells were incubated for 2 h in the dark, and the optical density value was measured using a microplate reader (Multiskan FC, Thermo Scientific, Germany).

2.7. Cellular uptake behavior of nanoparticles

The cellular uptake behavior of SLB NPs+IPI-549 NPs on 4T1 cells was evaluated using the CCK-8 assay. Because the raw material cannot spontaneously display fluorescence, it was marked with Nile red (NR) and fluorescein isothiocyanate (FITC green). 4T1 cells (1×10^5 cells/dish) were incubated in a Petri dish cell for 24 h. Afterwards, the cell culture solution was substituted by NPs containing equivalent amounts of PEG-PCL-FITC-IPI-549, PEG-PCL-NR-SLB, AEAA-PEG-PCL-FITC-IPI-549, and AEAA-PEG-PCL-NR-SLB, and the cells were incubated for an additional 0.5, 2 and 4 h. The culture solution was then removed, and the 4T1 cells were washed with PBS in duplicate. Then, 4% W/V formaldehyde was used to fix cells for 15 min, and the cells were washed with PBS again. Subsequently, the cell nuclei were stained with DAPI, and the cells were incubated for 10 min. The washed culture dish was then placed under CLSM (Zeiss LSM 700) to observe the fluorescence intensity and distribution in the cells.

2.8. Anti-tumor efficacy in mouse breast cancer cell (4T1) xenografts

After 7 days of adaptive feeding, an orthotopic tumor model was established. First, 4T1 cells were digested and resuspended in serum-free medium. Then, the cells were resuspended thrice with PBS buffer and diluted to 2×10^6 cells/mL. The cell suspension (200 μL) was inoculated subcutaneously into the right mammary glands of female balb/c mice using a disposable sterile syringe. On day 8 after tumor implantation (tumor size 50-70 mm^2), the mice were randomized into 7 groups (n = 5) as follows: untreated control (Saline); SLB (SLB in 30% PEG-400 solution, stirred or sonicated to evenly disperse, 5 mg/kg); SLB NPs; IPI-549 (IPI-549 in 30% PEG-400 solution, stirred or sonicated to evenly disperse, 5 mg/kg); IPI-549 NPs; SLB+IPI-549; and SLB NPs + IPI-549 NPs. Each sample solution was

prepared according to the preset concentration and the average mouse body weight and sterilized using a 0.45-μm sterile filter. The mice were administered the drug (200 μL/each) via the tail vein using a disposable sterile syringe every other day. Drug administration was performed 7 times in total. The tumor long axis and short axis were monitored using a Vernier caliper every other day and calculated as 1/2 × (long axis) × (short axis)^2. After 22 days of inoculation, the mice were sacrificed by cervical dislocation, and the tumor tissue and major organs were collected for further experiments. The inhibition ratio (IR) was calculated using IR (%) = [(Ws-Wt)/Ws] × 100, where Ws and Wt refer to average tumor weights for the saline group and each administration group, respectively.

2.9. Safety evaluation

The drug was administered 7 times in total, at an interval of once every other day. After 22 days of administration, all mice were sacrificed, and the heart, liver, spleen, lung and kidney of body were quickly dissected, placed in tissue bottles, and immobilized with formalin. Then, the morphology and pathology of the prepared tissues were studied by hematoxylin-eosin (H&E) staining, and the safety of the nanoparticles was evaluated. Briefly, the main organs were embedded in paraffin and sectioned, and the tissue sections were dewaxed and stained with H&E. Subsequently, images of the prepared tissues were observed using positive fluorescence microscopy (NIKON, Japan) to evaluate the safety of the nanoparticles.

2.10. TUNEL assay

The TUNEL assay was used to detect apoptotic cells in tumor tissues. After the mice were sacrificed, the intact tumors were dissected and fixed with formalin and sectioned; then, the tumor tissue was deparaffinized and stained with DAPI staining. Finally, the sections were washed with PBS, dried, and sealed with an anti-fluorescence quencher. Images were captured under a fluorescence microscope (NIKON, Japan) and quantitatively analyzed for apoptosis using Image Pro Plus 6.0.

2.11. Immunofluorescence staining

By double-labeling tumor tissue sections, protein expression in tissue cells was determined, and the anti-tumor mechanism in vivo was explored. Tumor sections were deparaffinized for rehydration to retrieve the antigen, naturally cooled, washed, and dried. Then, the sections were incubated for 30 min with 1% bovine serum albumin (BSA), and the primary antibody was incubated for 12 h at 4 °C. The next day, the sample was treated with a secondary antibody at room temperature for 50 min, and the nuclei were counterstained with DAPI. Finally, the sample image was observed and acquired using a fluorescence microscope (NIKON, Japan).

2.12.Masson trichrome staining

Collagen in tumor tissue was detected by Masson's trichrome assay. Tumor sections were deparaffinized and hydrated. The sections were then stained according to the manufacturer's instructions and finally differentiated and blocked. Collagen in tumor tissue of images was analyzed using a vertical optical microscope and imaged (NIKON, Japan).

2.13. Analysis of α-SMA and PARP expression using Western blot

The anti-tumor mechanism of this study was verified using Western blot assays. First, the tumor tissue was excised and mixed with the tissue lysate. Afterwards, the cell debris was cleared by centrifugation, and protein-loaded buffer was added to completely denature the protein. The sample was separated by SDS-PAGE, and the protein in the gel was transferred to a polyvinylidene fluoride (PVDF) membrane. Then, the membrane was covered with a blocking solution with agitation for 2 h and incubated with the indicated primary antibodies α-SMA, PARP, and GAPDH at 4 °C overnight. The membrane was thoroughly washed with TBST and blotted on a membrane strip, and the strip was placed in the secondary antibody working solution, incubated at RT for 2 h in the dark, and washed thoroughly with TBST. The PVDF membrane was placed face up between the two films of the exposed enamel, and the mixed ECL solution was added. After 1-2 min, the residual liquid was removed, and the film was covered to start exposure. Finally, the exposed film was developed and fixed, the archived film was scanned, the color was removed using Adobe Photoshop, and the optical density value was processed using grayscale analysis software (alpha EaseFC).

2.14. Statistical analysis

Quantitative data in the study are presented as the mean ± standard deviation (SD) using GraphPad for statistical analysis, and the difference analysis was performed using a one-way variance method. P values < 0.05 were considered significant as follows: *, P<0.05; **, P < 0.01; ***, P < 0.001.

3. Results and Discussion

3.1. Characterization of AEAA-PEG-PCL

The chemical structures of the products at each step were characterized using FT-IR spectra. Fig. 1 shows the infrared spectra of (A) NH_2-PEG-NH-Boc, (B) AEAA-PEG-NH-Boc, (C) AEAA-PEG-NH_2·TFA, and (D) AEAA-PEG-PCL. The NH_2-PEG-NH-Boc infrared spectrum (A) shows that the absorption peak at 3380 cm^{-1} and 2886 cm^{-1} is the stretching vibration of CH in the NH and PEG segments, and the absorption peak at 1711 cm^{-1} corresponds to the ester bond. The characteristic absorption peak is C=O.

Compared with Fig. 1A, the skeletal vibration absorption peak of the benzene ring appears in Fig. 1B; that is, the wavenumber is 1605 cm^{-1} and 1506 cm^{-1}, and the stretching vibration (1706 cm^{-1}) of C=O is shifted to the right, which indicates the successful synthesis of AEAA-PEG-NH-Boc.

Comparing C with B, the stretching vibration of C=O became 1681 cm^{-1}, indicating

that the tert-butoxycarbonyl group was successfully substituted.

In the D diagram, the absorption peaks at 1945 cm^{-1} and 2866 cm^{-1} are the CH stretching vibrations of the PEG and PCL segments, respectively, and the absorption peak at 1724 cm^{-1} belongs to the C=O vibration of the PCL segment. These characteristic absorption peaks indicate that PCL was successfully bonded to AEAA-PEG-NH_2·TFA. In addition to the FT-IR spectra, the 1H NMR also clearly affirmed the successful conjugations of AEAA-PEG-NH-Boc, AEAA-PEG-NH_2·TFA, and AEAA-PEG-PCL (Fig. 2). As shown in Fig. 2, the nuclear magnetic resonance spectrum of Fig. 2A shows that the peak is assigned to its molecular structure, and the proton peak signal in the range of 2.89-3.62 ppm belongs to the hydrogen on the PEG segment. The proton peak signal at 1.37 ppm corresponds to the methyl peak of the tert-butoxycarbonyl group (Boc) at one end of the PEG, and the proton peak signal at 6.73 ppm is attributed to the hydrogen proton on the amino group at the other end of the PEG. In Fig. 2B, the new proton signal peak at 8.57 ppm is the hydrogen proton signal on the amino group directly attached to the carbonyl group, while the signal peak at 8.0 and 7.8 ppm is derived from the benzene ring structure of AEAA. The methyl peak of the tert-butoxycarbonyl group (Boc) in C disappeared, which confirms the successful synthesis of AEAA-PEG-NH_2.

The proton peak signals of 1.27, 1.55, 2.27, and 3.98 ppm appearing in Fig. 2D are attributed to hydrogen on the PCL segment, indicating the successful synthesis of the targeting vector AEAA-PEG-PCL.

3.2. Characterization of nanoparticles

A nanoparticle-based drug delivery system is an effective method to target the delivery of hydrophobic therapeutics to tumor sites (Wang and Thanou, 2010). Therefore, water-insoluble IPI-549 and SLB were encapsulated into NPs using the solvent displacement method so that improve drug solubilization and enhance drug targeting after systemic administration. As a result, the EE for IPI-549 NPs and SLB NPs was 91.4 ± 3.8% and 76.9 ± 0.2%, respectively, and the DL for IPI-549 NPs and SLB NPs was 15.8 ± 6.4% and 12.9 ± 7.1%, respectively. The average sizes of IPI-549 NPs (Fig. 3A) and SLB NPs (Fig. 3B) were 34.4 nm and 37.2 nm, respectively, measured by DLS. As shown in Figs. 3 (C-D), there are spherical configuration and relatively uniform size of these nanoparticles by TEM measurement. Meanwhile, the CMC for the AEAA-PEG-PCL NPs were also measured (2.41 μg/mL) (Fig. 4A).

3.3. Study on the *in vitro* release properties of nanoparticles

The release of IPI-549 and SLB from the NPs exhibited a different maximum cumulative release (37.25% and 74.13%) at the same time (45 h) in pH 7.4 (Fig. 4B). The results showed that both nanoparticle formulations had a very large sustained release effect, which significantly prolonged the time of activity of SLB and IPI-549 and improving the bioavailability of the two drugs. In addition, the difference in the release rates of the two nanoparticles is mainly due to the extremely

poor water solubility of IPI-549.

3.4. Cell toxicity and *in vitro* synergistic effects

We first determined the toxicity of the empty carrier PEG-PCL and the targeting vector AEAA-PEG-PCL on murine breast cancer cells (4T1 cells). The results showed that both vectors were biosafe. As shown in Fig. 5, after a 24-h incubation with different concentrations of PEG-PCL solution and AEAA-PEG-PCL solution, the toxicity of 4T1 cells was negligible. After 48 h, the targeting vector was less toxic than PEG-PCL. The results of these studies indicate that the target carrier of this study has good biosafety, which also plays an important role in maintaining the low toxicity and side effects of NPs in systemic circulation.

The cell inhibition effect of SLB and IPI-549 and their NPs was evaluated (Fig. 5). Both SLB and IPI-549 reduced the survival rate of 4T1 cells, exhibiting good concentration-dependent and time-dependent effects. The antitumor effects of NPs were significantly stronger than that of the free drugs. SLB NPs + IPI-549 NPs had the highest cytotoxicity, which showed that the combined treatment was synergistic and had a powerful inhibitory effect on tumor cells.

3.5. Cellular uptake of nanoparticles

Aminoethyl anisamide enhances the cellular uptake of nanoparticles by specifically binding to sigma receptors on the surface of tumor cells(Kim et al., 2018). Fig. 6 shows representative CLSM images of 4T1 cells incubated with AEAA-PEG-PCL-IPI-549 NPs and AEAA-PEG-PCL-SLB NPs loaded with FITC and NR for 4 h. With increasing incubation time, strong red and green fluorescence signals were observed at the periphery of the cell nucleus, indicating that the nanoparticles were effectively absorbed by the cells, thus validating the efficacy of our therapeutic system for 4T1 cell delivery. To demonstrate the targeting ability of nanoparticles, surface-unmodified PEG-PCL-FITC-IPI-549 and PEG-PCL-NR-SLB were also incubated with 4T1 cells for 4 h. We can observe clearly that the red and green fluorescence of 4T1 cells was relatively lower at each time point. The results showed that the surface modification of NPs to aminoethyl anisamide significantly promoted their cellular uptake in 4T1 cells.

3.6. Anti-tumor efficacy in mouse breast cancer cells (4T1) xenografts

The effects of drug-loaded nanoparticles on tumor growth were assessed. As shown in Fig. 7A, the tumor growth rate was extremely rapid (approximately 1700 mm^3 on the 16th day) in the control group. The SLB showed a less curative effect than the IPI-549 drug at the same dose. Notably, the antitumor effects of SLB NPs and IPI-549 NPs were significantly stronger, which is consistent with the results of the cell toxicity experiments. The combined action of SLB NPs and IPI-549 NPs resulted in the strongest tumor inhibition effect, in which the tumor volume was only approximately 350 mm^3 after 16 days of treatment. As shown in Fig. 7C, SLB NPs+IPI-549 NPs significantly inhibited transplanted tumor growth in mice, and the tumor weight (0.4 g) was lighter than that of the control group (2.6 g) ($P <$

0.001). The average inhibition rate of each group was compared, and the SLB inhibition rate was 26.92%. The inhibition rates of SLB NPs, IPI-549, and IPI-549 NPs were 61.5%, 50% and 69.23%, respectively, which were comparable to that of SLB+IPI-549 (57.69%). The inhibition rate of SLB NPs+IPI-549 NPs treatment reached 84.62%, indicating that the therapeutic effect of the combined administration of SLB NPs and IPI-549 NPs was improved. The tumor weight and tumor volume results showed that the SLB NPs+IPI-549 NP treatment had strong anti-tumor ability and high activity *in vivo*.

3.7. Safety evaluation of the different treatments

The mice treated with different drug formulations had no abnormal changes in body weight throughout the tumor inhibition experiment (Fig. 8A). In addition, the H&E staining observations indicated no obvious pathological changes in the hearts, spleens, lungs, and kidneys (Fig. 8B). These findings confirmed that the NP structures are safe to animals.

3.8. TUNEL assay

The tumor cell apoptosis index was quantitatively analyzed using a TUNEL assay. The tumor cells in the control group exhibited very little apoptosis, while the tumor cells in the mice treated with drugs exhibited different degrees of apoptosis. Notably, the tumor tissue showed the highest level of cell apoptosis (46.6 ±2.7%) in the SLB NPs + IPI-549 NPs group (Fig. 9). These results are associated with the tumor inhibition data, indicating that the optimal therapeutic effect is produced by the combined nanoparticles. This finding might be attributed to the synergistic effect and the targeted release of the drug.

3.9. Suppression of cell reprogramming in the TEM

AEAA-PEG-PCL-SLB NPs and AEAA-PEG-PCL-IPI-549 NPs can efficiently deliver SLB and IPI-549 to tumor cells. Immunoregulatory cell populations, including MDSCs, TFA, and Treg cells, were investigated during the experiments. These cells secrete various cytokines and chemokines to affect tumor cells (Song et al., 2018). Treg cells are a subset of CD4 + T cells with immunosuppressive effects that play a key role in the homeostasis of maintaining immune cells, and their specific transcription factor Foxp3 (forkhead/winged helix transcription factor3) is mainly expressed in the nucleus of lymphocytes (Li and Wang, 2012; Ohta et al., 2012). Foxp3 also plays an important role in regulating the differentiation, development and function of Tregs and is recognized as a Treg-specific marker (Bacchetta et al., 2007; Shi and Sun, 2014). MDSCs exert immunosuppressive functions through multiple pathways and mechanisms, and the phenotypic marker of mouse MDSCs is CD11b + Gr-1 (Yang et al., 2015). The results (Fig. 10) show that the percentage of MDSCs and Treg cells in the TME is reduced after SLB treatment. The inhibitory effect of silibinin on MDSCs and Tregs in a mouse model of breast cancer is consistent with the results of the previous study (Castellaneta et al., 2016). Forghani et al. also reported that SLB failed to

inhibit tumor growth in immunodeficient mice, indicating that the anticancer effects of SLB are immune-mediated (Forghani et al., 2014). However, when SLB was combined with IPI-549, the MDSC and Treg cell counts were significantly reduced even lower than those in the SLB-treated and IPI-549-treated groups. This result is because IPI-549 can not only alter the immunosuppressive microenvironment of tumors but can also trigger an anti-tumor immune response (Pathria et al., 2019). Therefore, in present study, the anti-tumor immune response is further activated by both enhancing the anti-tumor immunosuppressive effect and its tumor-suppressive activity in the SLB NPs + IPI-549 NPs group (Fig. 10B-E). Taken together, our data suggest that SLB and IPI-549 have synergistic effects in anti-tumor immunosuppression.

3.10. Structural changes in the TME: TAFs, vasculature, and collagen fibers

TAFs are considered a class of cells that promote tumor cell growth and metastasis through multiple pathways and can inhibit anti-tumor immune responses (Costa et al., 2018; Wang et al., 2012). The effect of SLB NPs on TAFs was investigated by staining for α-smooth muscle actin (α-SMA) (a TAF biomarker) (Lin et al., 2018). The results indicated that both SLB and SLB NP treatments remarkably decreased TAF expression in tumors (Fig. 10A), which is consistent with the results that SLB demonstrated antifibrotic properties (Trappoliere et al., 2009). Furthermore, the combination of SLB and IPI-549 NPs reduced the percentage of fibroblasts in the tumor to 18.0 ± 3.0% ($p < 0.001$) (Fig. 10B). Abnormal vessel structures cause malignant cells to migrate and prevent drug and immunocyte penetration into the tumor mass, which further enhance the deterioration of tumor cells. We evaluated the vascular content and distribution in tumors by immunohistochemistry of CD31 (vascular marker) in each group (Fig. 10A). Both SLB NPs and IPI-549 NPs dramatically reduced the percentage of vascular content to 33.3 ± 7.7% and 30.5 ± 7.1% ($p < 0.01$), respectively. The combined drug treatment exhibited the lowest blood vessel content of 14.7 ± 3.8% ($p < 0.001$). These data suggest that SLB and IPI-549 caused structural changes in the TME, facilitating the reconstitution of fibroblasts and the vascular network.

Similarly, SLB NPs + IPI-549 NPs also significantly reduced the matrix content of the tumor mass. We examined collagen content and distribution as well as morphology in the tumor by Masson trichrome staining (Fig. 11). The matrix of collagen staining exhibited a relatively slender fibrous structure in the control tumor. The IPI-549 NPs reduced the matrix to only 66.3 ± 7.1% ($p < 0.01$) of that in the control group, while the SLB NPs reduced the matrix by approximately 33.0 ± 1.9% ($p < 0.001$) of the untreated control. Thus, the powerful effect of SLB on collagen in present study is consistent with the report that SLB retards collagen accumulation fibrosis induced in rats (Boigk et al., 1997). In the SLB NPs + IPI-549 NPs group, the collagen content was further reduced to only approximately 23.0 ± 4.8% ($p < 0.001$). Therefore, we conclude that SLB NPs + IPI-549 NPs exert topgallant anti-tumor efficiency via antifibrotic, angiogenesis suppression, and inhibition of tumor cell migration, attributing to the synergistic effect of drugs.

3.11. Analysis of α-SMA and PARP expression using Western blot

The results are shown in Fig. 12A. Compared with the untreated tumor, SLB NPs + IPI-549 NPs dramatically reduced the expression levels of the downstream cleavage of poly ADP ribose polymerase (PARP) (apoptosis marker), which were relatively lower than those induced by SLB/IPI-549 NPs and free SLB/IPI-549. This finding is consistent with the TUNEL data. α-SMA expression was reduced in tumors in the SLB NPs and SLB NPs + IPI-549 NPs groups. The results showed that SLB has an anti-fibrotic effect and can effectively inhibit TAF production. The combination of SLB and the IPI-549 significantly improved the TME, inhibiting breast cancer cell aggregation.

4.Conclusion

In this study, a long-circulating nanoparticle system based on tumor targeting was designed for breast cancer by immunotherapy. This nanoparticle system had a "core-shell" structure containing a hydrophobic IPI-549/SLB nanocore and a hydrophilic AEAA-PEG-PCL targeted shell and achieved both the efficient targeting of breast tumors and the slow release of IPI-549 and SLB. In the TME, IPI-549 and SLB decreased the amount of MDSCs and Treg cells and altered the blood vessel and stromal structure of the tumor. IPI-549 enhanced the immune-mediated anti-cancer effect from SLB by modulating immunosuppressive cells. Our data provided evidence *in vivo* and *in vitro* that the codelivery of PI3Kγ inhibitors and an anti-fibrotic drug to tumors can act synergistically by remodeling the TME in breast cancer, which improves the oncotherapy efficiency of existing therapies.

Conflict of interest

The authors declare that they have no conflicts of interest.

References

Bacchetta, R., Gambineri, E., Roncarolo, M.G., 2007. Role of regulatory T cells and FOXP3 in human diseases. J Allergy Clin Immunol 120, 227-235.

Boigk, G., Stroedter, L., Herbst, H., Waldschmidt, J., Riecken, E.O., Schuppan, D., 1997. Silymarin retards collagen accumulation in early and advanced biliary fibrosis secondary to complete bile duct obliteration in rats. Hepatology 26, 643-649.

Castellaneta, A., Massaro, A., Rendina, M., D'Errico, F., Carparelli, S., Rizzi, S.F., Thomson, A.W., Di Leo, A., 2016. Immunomodulating effects of the anti-viral agent Silibinin in liver transplant patients with HCV recurrence. Transplantation research 5, 1.

Costa, D., Venè, R., Benelli, R., Romairone, E., Scabini, S., Catellani, S., Rebesco, B., Mastracci, L., Grillo, F., Minghelli, S., 2018. Targeting the Epidermal Growth Factor Receptor Can Counteract the Inhibition of Natural Killer Cell Function Exerted by Colorectal Tumor-Associated Fibroblasts. Front Immunol 9, 1150.

De Henau, O., Rausch, M., Winkler, D., Campesato, L.F., Liu, C., Cymerman, D.H., Budhu, S., Ghosh, A., Pink, M., Tchaicha, J., 2016. Overcoming resistance to checkpoint blockade therapy by targeting PI3Kγ in myeloid cells. Nature 539, 443.

Evans, C.A., Liu, T., Lescarbeau, A., Nair, S.J., Grenier, L., Pradeilles, J.A., Glenadel, Q., Tibbitts, T., Rowley, A.M., DiNitto, J.P., 2016. Discovery of a selective phosphoinositide-3-kinase (PI3K)-γ inhibitor (IPI-549) as an immuno-oncology clinical candidate. ACS medicinal chemistry letters 7, 862-867.

Forghani, P., Khorramizadeh, M.R., Waller, E.K., 2014. Silibinin inhibits accumulation of myeloid-derived suppressor cells and tumor growth of murine breast cancer. Cancer Medicine 3, 215-224.

Francoa, P.I.R., Rodrigues, A.P., de Menezes Leite, L.B., Miguel, M.P., 2019. Tumor microenvironment components: Allies of cancer progression. Pathology-Research and Practice, 152729.

Franklin, R.A., Liao, W., Sarkar, A., Kim, M.V., Bivona, M.R., Liu, K., Pamer, E.G., Li, M.O., 2014. The cellular and molecular origin of tumor-associated macrophages. Science 344, 921-925.

Gao, P., Han, X., Zhang, Q., Yang, Z., Fuss, I.J., Myers, T.G., Gardina, P.J., Zhang, F., Strober, W., 2014. Dynamic changes in E-protein activity regulate T reg cell development. Journal of Experimental Medicine 211, 2651-2668.

Hammam, O.A., El, W.H., 2012. Anti-inflammatory/anti-fibrotic effects of the hepatoprotective silymarin and the schistosomicide praziquantel against Schistosoma mansoni-induced liver fibrosis. Parasites & Vectors 5: art.no.9. Parasit Vectors 5, 9-9.

He, H.Y., Qi, L.Y., Xiao, Y.S., Hou, Y., 2017. Tumor Associated Fibroblasts Promote PD-L1 Expression in Lung Cancer Cells. Chinese Journal of Lung Cancer 20, 293-297.

Hossainzadeh, S., Ranji, N., Naderi Sohi, A., Najafi, F., 2019. Silibinin encapsulation in polymersome: A promising anticancer nanoparticle for inducing apoptosis and decreasing the expression level of miR - 125b/miR - 182 in human breast cancer cells. Journal of cellular physiology 234, 22285-22298.

Hou, L., Liu, Q., Shen, L., Liu, Y., Zhang, X., Chen, F., Huang, L., 2018. Nano-delivery of fraxinellone remodels tumor microenvironment and facilitates therapeutic vaccination in desmoplastic melanoma. Theranostics 8, 3781.

Houthuijzen, J., Jonkers, J., 2018. Cancer-associated fibroblasts as key regulators of the breast cancer tumor microenvironment. Cancer and Metastasis Reviews 37, 577-597.

Huo, M., Zhao, Y., Satterlee, A.B., Wang, Y., Xu, Y., Huang, L., 2017. Tumor-targeted delivery of sunitinib base enhances vaccine therapy for advanced melanoma by remodeling the tumor microenvironment. Journal of controlled release 245, 81-94.

Janku, F., 2017. Phosphoinositide 3-kinase (PI3K) pathway inhibitors in solid tumors: From laboratory to patients. Cancer treatment reviews 59, 93-101.

Ko, J.-W., Shin, N.-R., Park, S.-H., Lee, I.-C., Ryu, J.-M., Kim, H.-J., Cho, Y.-K., Kim, J.-C., Shin, I.-S., 2017. Silibinin inhibits the fibrotic responses induced by cigarette smoke via suppression of TGF-β1/Smad 2/3 signaling. Food and Chemical Toxicology 106, 424-429.

Lei, A.H., Zhou, J., 2014. Recent Progress on MDSCs and Tumor Immune Tolerance. Progress in Biochemistry & Biophysics 41, 58-68.
Li, B., Wang, R.F., 2012. Mechanisms and Control of Regulatory T Cells in Cancer.
Lin, G., Chen, S., Mi, P., 2018. Nanoparticles targeting and remodeling tumor microenvironment for cancer theranostics. Journal of biomedical nanotechnology 14, 1189-1207.
Liu, M., Song, W., Huang, L., 2019. Drug delivery systems targeting tumor-associated fibroblasts for cancer immunotherapy. Cancer letters 448, 31-39.
Mi, P., Cabral, H., Kataoka, K., 2019. Ligand‐Installed Nanocarriers toward Precision Therapy. Advanced Materials, 1902604.
Ohta, A., Kini, R., Ohta, A., Subramanian, M., Madasu, M., Sitkovsky, M., 2012. The development and immunosuppressive functions of CD4+ CD25+ FoxP3+ regulatory T cells are under influence of the adenosine-A2A adenosine receptor pathway. Frontiers in Immunology 3, 190-190.
Pathria, P., Louis, T.L., Varner, J.A., 2019. Targeting tumor-associated macrophages in Cancer. Trends in immunology.
Polachi, N., Bai, G., Li, T., Chu, Y., Wang, X., Li, S., Gu, N., Wu, J., Li, W., Zhang, Y., 2016. Modulatory effects of silibinin in various cell signaling pathways against liver disorders and cancer–A comprehensive review. European journal of medicinal chemistry 123, 577-595.
Shi, L., Sun, X., 2014. Advances in Study on Correlation between Foxp3~+ Regulatory T Cells and Colorectal Cancer. Chinese Journal of Gastroenterology 19, 57-60.
Siegel, R.L., Miller, K.D., Jemal, A., 2019. Cancer statistics, 2019. CA: A Cancer Journal for Clinicians 69, 7-34.
Song, Y., Tang, C., Yin, C., 2018. Combination antitumor immunotherapy with VEGF and PIGF siRNA via systemic delivery of multi-functionalized nanoparticles to tumor-associated macrophages and breast cancer cells. Biomaterials 185, 117-132.
Trappoliere, M., Caligiuri, A., Schmid, M., Bertolani, C., Failli, P., Vizzutti, F., Novo, E., Manzano, C.D., Marra, F., Loguercio, C., 2009. Silybin, a component of sylimarin, exerts anti-inflammatory and anti-fibrogenic effects on human hepatic stellate cells ☆. Journal of Hepatology 50, 1102-1111.
van Waarde, A., Rybczynska, A.A., Ramakrishnan, N.K., Ishiwata, K., Elsinga, P.H., Dierckx, R.A., 2015. Potential applications for sigma receptor ligands in cancer diagnosis and therapy. Biochimica et Biophysica Acta (BBA)-Biomembranes 1848, 2703-2714.
Vlachou, K., Fanouriakis, A., Glymenaki, M., Ioannou, M., Mastorodemos, V., Verginis, P., Boumpas, D., 2012. Defects within the myeloid derived supressor cells (MDSCS) compartment may facilitate aberrant immune responses in systemic lupus erythematosus (SLE). Annals of the Rheumatic Diseases 71, A84-A85.
Wallecha, A., Singh, R., Malinina, I., 2013. Listeria monocytogenes (Lm)-LLO immunotherapies reduce the immunosuppressive activity of myeloid-derived suppressor cells and regulatory T cells in the tumor microenvironment. Journal of immunotherapy 36, 468-476.

Wang, D., Wang, S., Shi, C., 2012. Update on cancer related issues of mesenchymal stem cell-based therapies. Current stem cell research & therapy 7, 370-380.
Weed, D.T., Vella, J.L., Reis, I.M., Adriana, C., Gomez, C., Sargi, Z., Nazarian, R., Califano, J., Borrello, I., Serafini, P., 2015. Tadalafil reduces myeloid-derived suppressor cells and regulatory T cells and promotes tumor immunity in patients with head and neck squamous cell carcinoma. Clinical Cancer Research 21, 39-48.
Yang, Z., Wu, T., Shao, S., Shi, B., Yong, Z., 2015. The phenotype, development and biological function of myeloid-derived suppressor cells. Oncoimmunology 5, 00-00.
Yu, M., Duan, X., Cai, Y., Zhang, F., Jiang, S., Han, S., Shen, J., Shuai, X., 2019. Multifunctional Nanoregulator Reshapes Immune Microenvironment and Enhances Immune Memory for Tumor Immunotherapy. Advanced Science, 1900037.
Zhang, X., Shen, L., Liu, Q., Hou, L., Huang, L., 2019. Inhibiting PI3 kinase-γ in both myeloid and plasma cells remodels the suppressive tumor microenvironment in desmoplastic tumors. Journal of Controlled Release 309, 173-180.
Zhao, Y., Huo, M., Xu, Z., Wang, Y., Huang, L., 2015. Nanoparticle delivery of CDDO-Me remodels the tumor microenvironment and enhances vaccine therapy for melanoma. Biomaterials 68, 54-66.

Figure Captions

Scheme 1. Schematic illustration of establishing a mouse xenograft tumor model and treatment by the tail vein injection of SLB NPs and IPI-549 NPs

Scheme 2. Schematic illustration of the synthesis of the AEAA-PEG-PCL conjugate.

Fig. 1. FT-IR characterization: (A) NH2-PEG-NH-Boc; (B) AEAA-PEG-NH-Boc; (C) AEAA-PEG-NH_2·TFA; (D) AEAA-PEG-PCL.

Fig. 2. ^{1}H NMR spectra of (A) NH2-PEG-NH-Boc; (B) AEAA-PEG-NH-Boc; (C) AEAA-PEG-NH_2·TFA; (D) AEAA-PEG-PCL.

Fig. 3. TEM images of (A) AEAA-PEG-PCL-IPI-549 NPs and (B) AEAA-PEG-PCL-SLB NPs. DLS histograms of (C) AEAA-PEG-PCL-IPI-549 NPs and (D) AEAA-PEG-PCL-SLB NPs.

Fig. 4. The critical micell concentration of AEAA-PEG-PCL NPs (A). In vitro cumulative release profiles of IPI-549 NPs and SLB NPs in PBS (pH 7.4) containing 0.1% (w/v) poloxamer at 37 °C (B). The results are presented as the mean ± SD (n = 3).

Fig. 5. Viability of 4T1 cells incubated with PEG-PCL and AEAA-PEG-PCL for 24 h (A) and 48 h (B). Viability of 4T1 cells incubated with SLB, SLB NPs, IPI-549, IPI-549 NPs, SLB+IPI-549 and SLB NPs+IPI-549 NPs for 24 h (A) and 48 h (B). The results are presented as the mean ± SD. (n = 6, * $P < 0.05$, ** $P < 0.01$, *** $P < 0.001$).

Fig. 6. CLSM images of 4T1 cells were incubated with (A) PEG-PCL NPs and (B) AEAA-PEG-PCL NPs for 0.5 h, 2 h, and 4 h. Scale bar = 20 μm.

Fig. 7. Tumor inhibition effects of SLB, SLB NPs, IPI-549, IPI-549 NPs, SLB+IPI-549, and SLB NPs+IPI-549 NPs on 4T1-bearing mice. 4T1-bearing mice were injected intravenously every other day at a dose of 5 mg/kg SLB/SLB NPs or 5 mg/kg IP-549/IPI-549 NPs in all treatment groups. (A) The tumor volumes curves of 4T1-bearing mice along the experiment duration by measured every other day. (B) Images of the excised tumors from each group at the end of the tumor inhibition experiment. (C) The IR and the average tumor weight of each treatment group at the end of the point (day 22). The results are presented as the mean ± SD. (n = 5, * $P < 0.05$, ** $P < 0.01$, *** $P < 0.001$).

Fig. 8. Safety evaluation of all treatment groups. (A) The average body weight curves of 4T1-bearing mice over the course of the experiment as measured every other day. (B) Representative H&E stained sections of major organs after treatment. Scale bar = 100 μm.

Fig. 9. Representative TUNEL-stained sections of tumors from each group after treatment. Tumor tissues were stained for cell apoptosis (green). Quantitative analysis of apoptotic index (TUNEL-positive cells/total cells). Scale bar = 100 μm. The results are presented as the mean ± SD. (n = 3, * $P < 0.05$, ** $P < 0.01$, *** $P < 0.001$).

Fig. 10. Remodeling of tumor-infiltrating immune cells in the TME. Tumor tissues were assayed for the blood vessel (CD31 in green) and tumor-associated fibroblasts (α-SMA in red), MDSC cells (Gr-1^+ in red, $CD11b^+$ in green), and Treg cells (CD4 in red, Foxp3 in green) with immunofluorescence staining (A). Flow cytometric

analysis was also used to quantify immune cells in the TME (B-E). Scale bar = 100 μm. The results are presented as the mean ± SD. (n = 3, * P < 0.05, ** P < 0.01, *** P < 0.001).

Fig. 11. Tumor sections were stained with Masson trichrome. The blue color represents collagen fibers. Scale bar = 100 μm. The results are presented as the mean ± SD. (n = 3, * P < 0.05, ** P < 0.01, *** P < 0.001).

Fig. 12. Western blot analysis assessment of α-SMA and PARP knockdown in tumor tissues after different treatments. The results are presented as the mean ± SD. (n = 3, * P < 0.05, ** P < 0.01, *** P < 0.001).

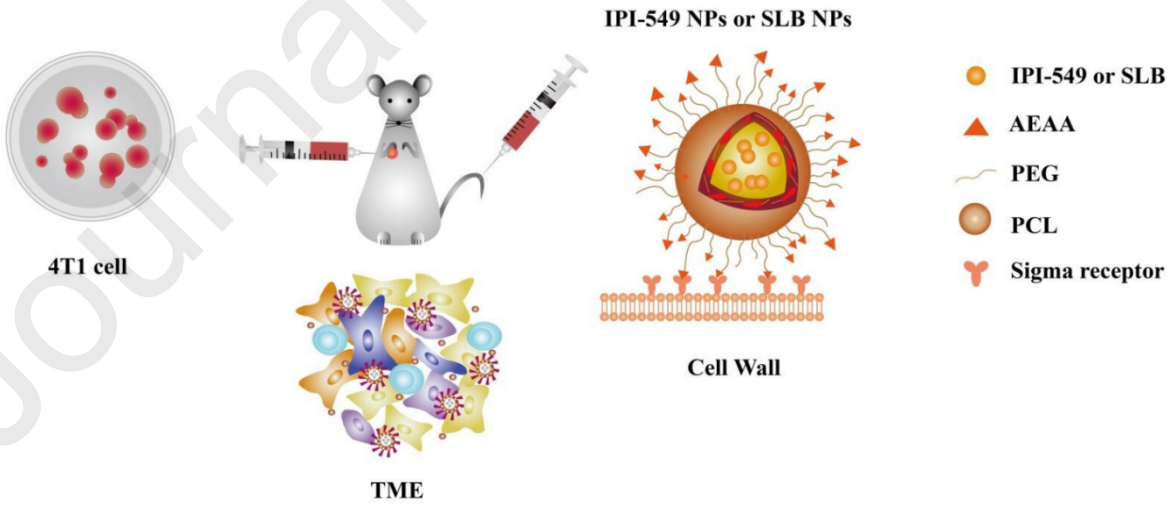

Scheme 1

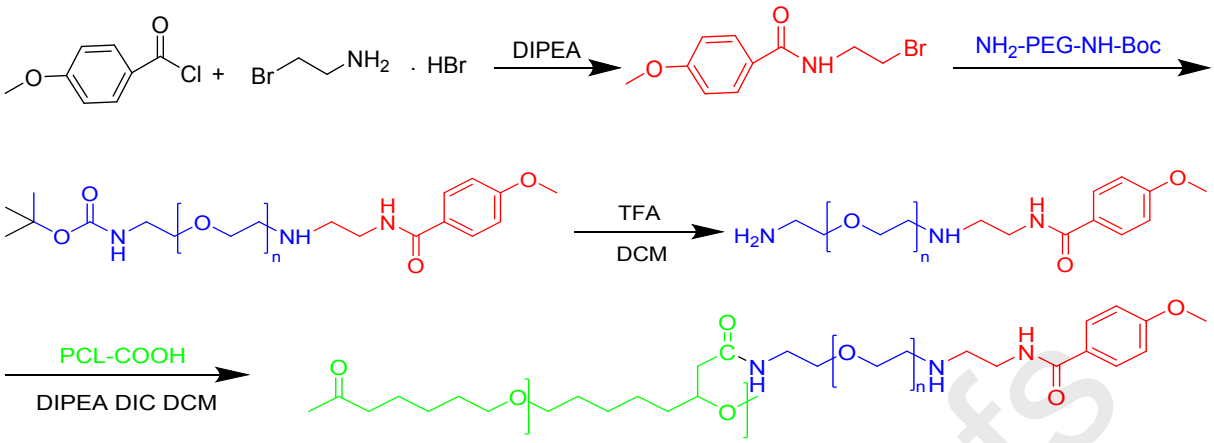

Scheme 2

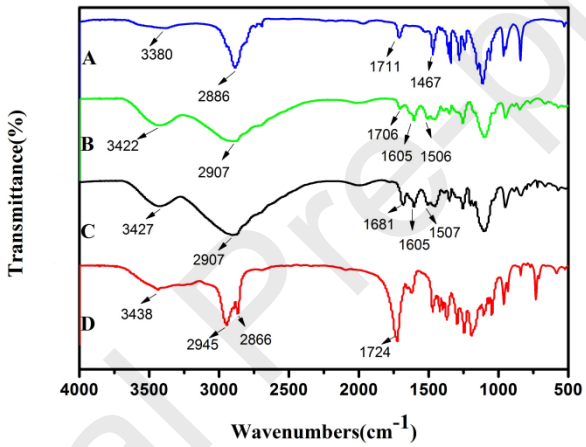

Fig. 1

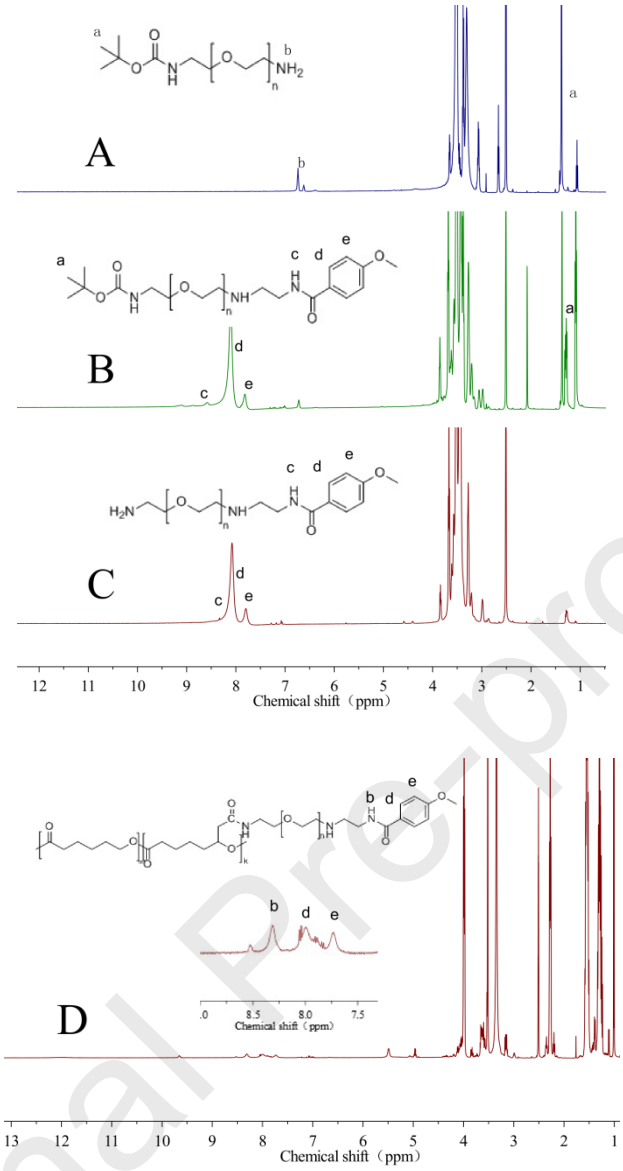

Fig. 2

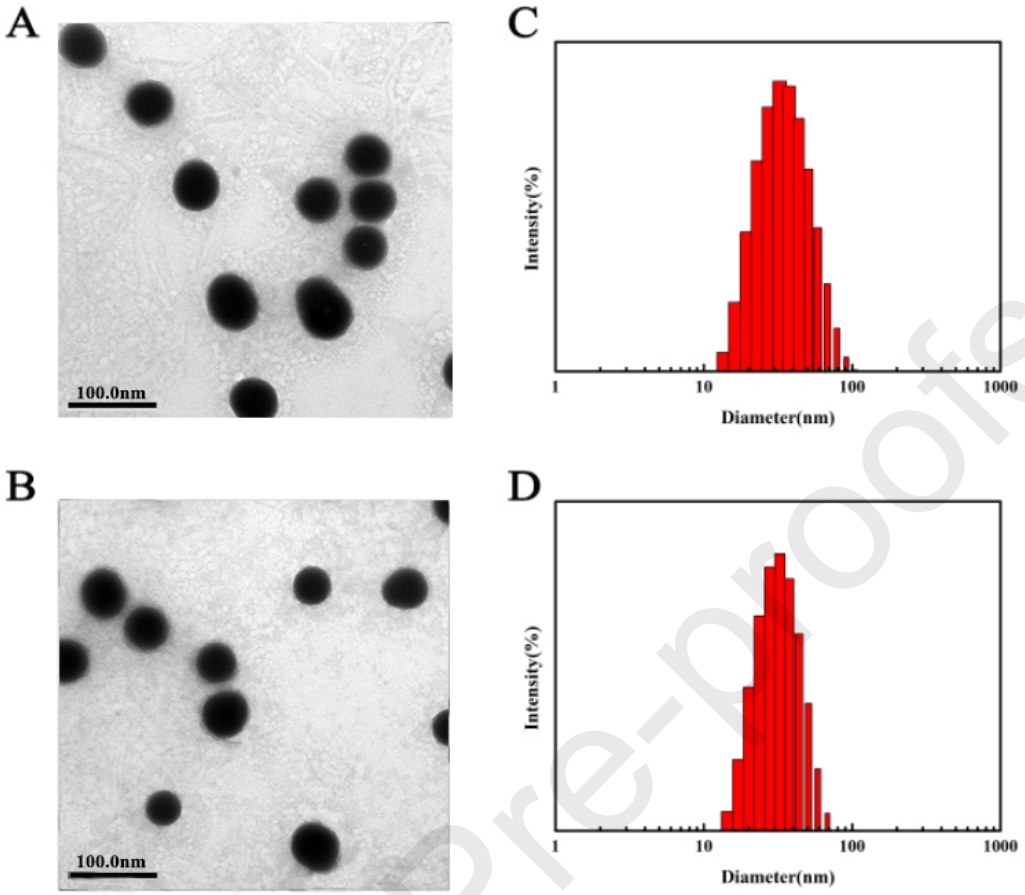

Fig. 3

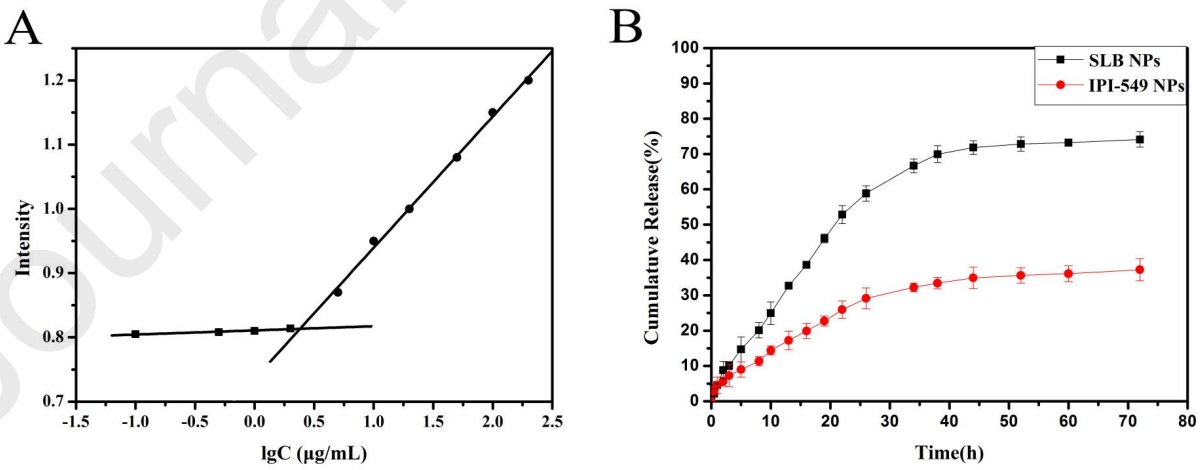

Fig. 4

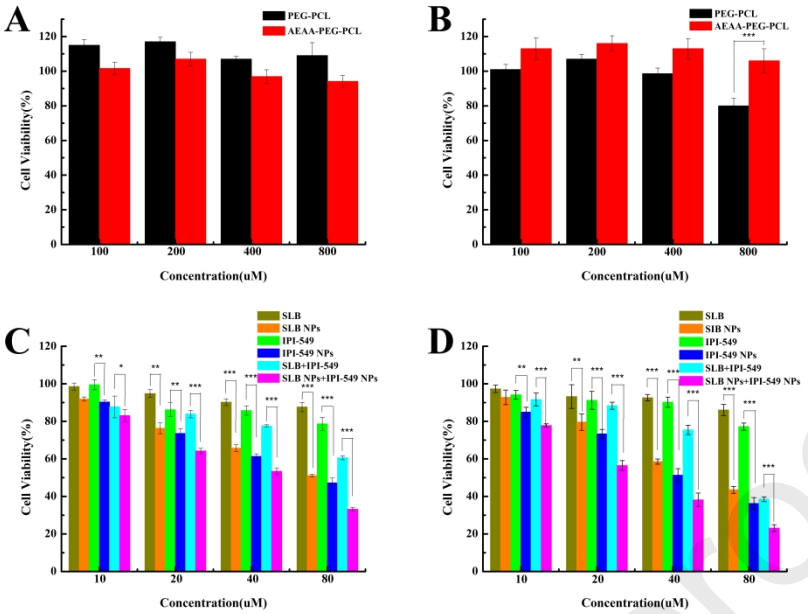
A
B
C
D
PEG-PCL
AEAA-PEG-PCL
Cell Viability(%)
Concentration(uM)
SLB
SLB NPs
IPI-549
IPI-549 NPs
SLB+IPI-549
SLB NPs+IPI-549 NPs

Fig. 5

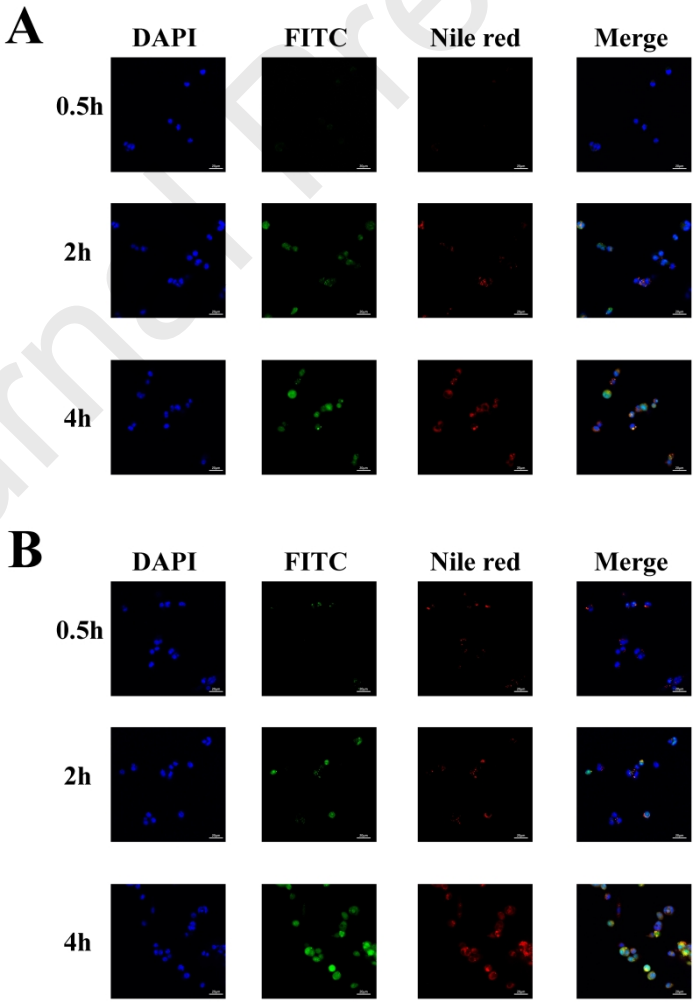
A
B
DAPI
FITC
Nile red
Merge
0.5h
2h
4h

Fig. 6

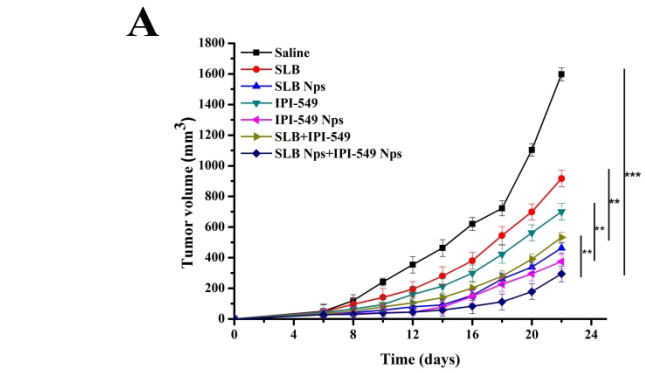

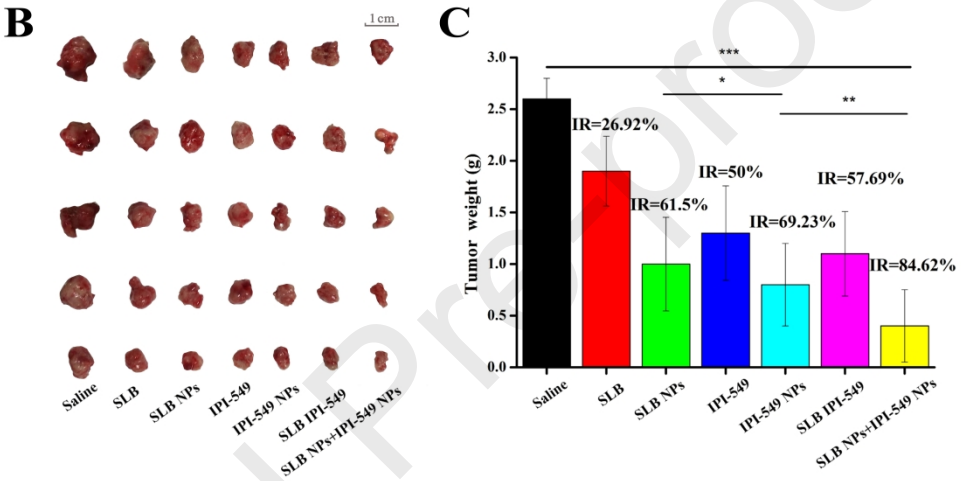

Fig. 7

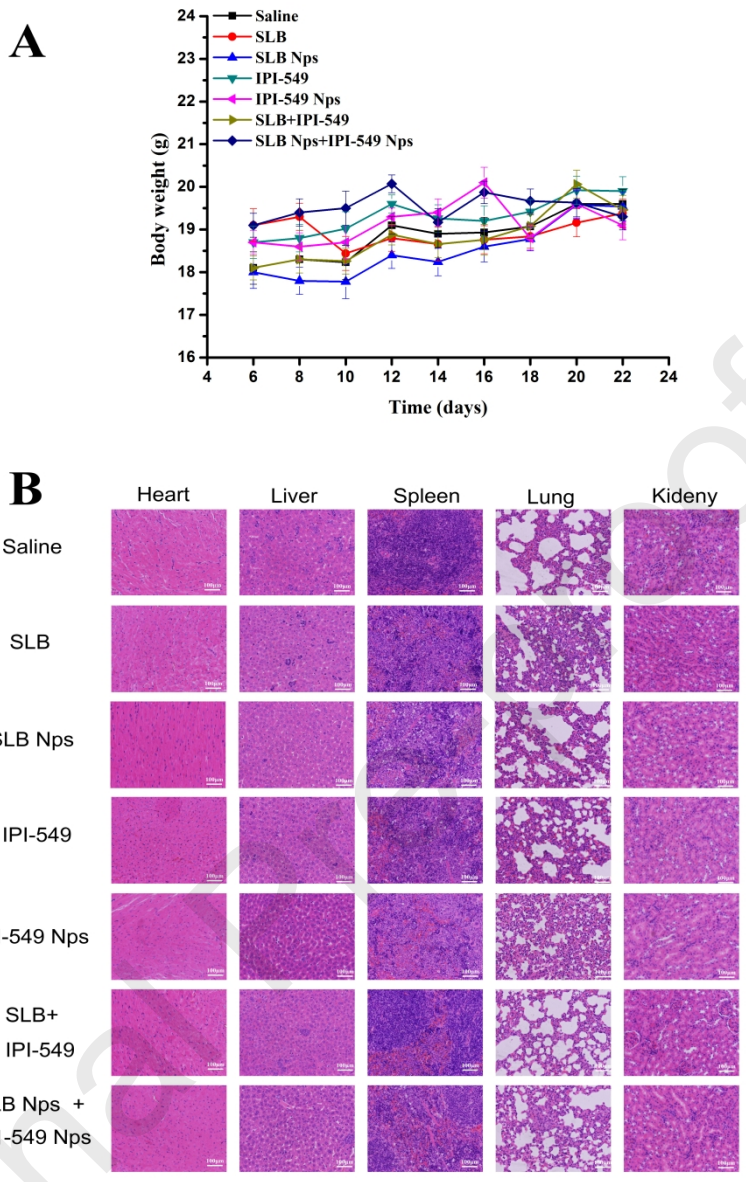
A
Saline
SLB
SLB Nps
IPI-549
IPI-549 Nps
SLB+IPI-549
SLB Nps+IPI-549 Nps
Body weight (g)
Time (days)
B
Heart
Liver
Spleen
Lung
Kideny
Saline
SLB
SLB Nps
IPI-549
IPI-549 Nps
SLB+
IPI-549
SLB Nps +
IPI-549 Nps

Fig. 8

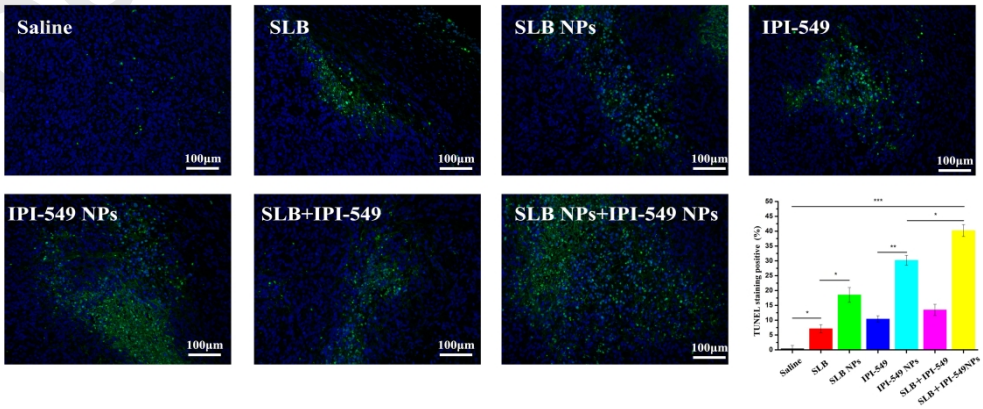
Saline
SLB
SLB NPs
IPI-549
IPI-549 NPs
SLB+IPI-549
SLB NPs+IPI-549 NPs
100μm
TUNEL staining positive (%)

Fig. 9

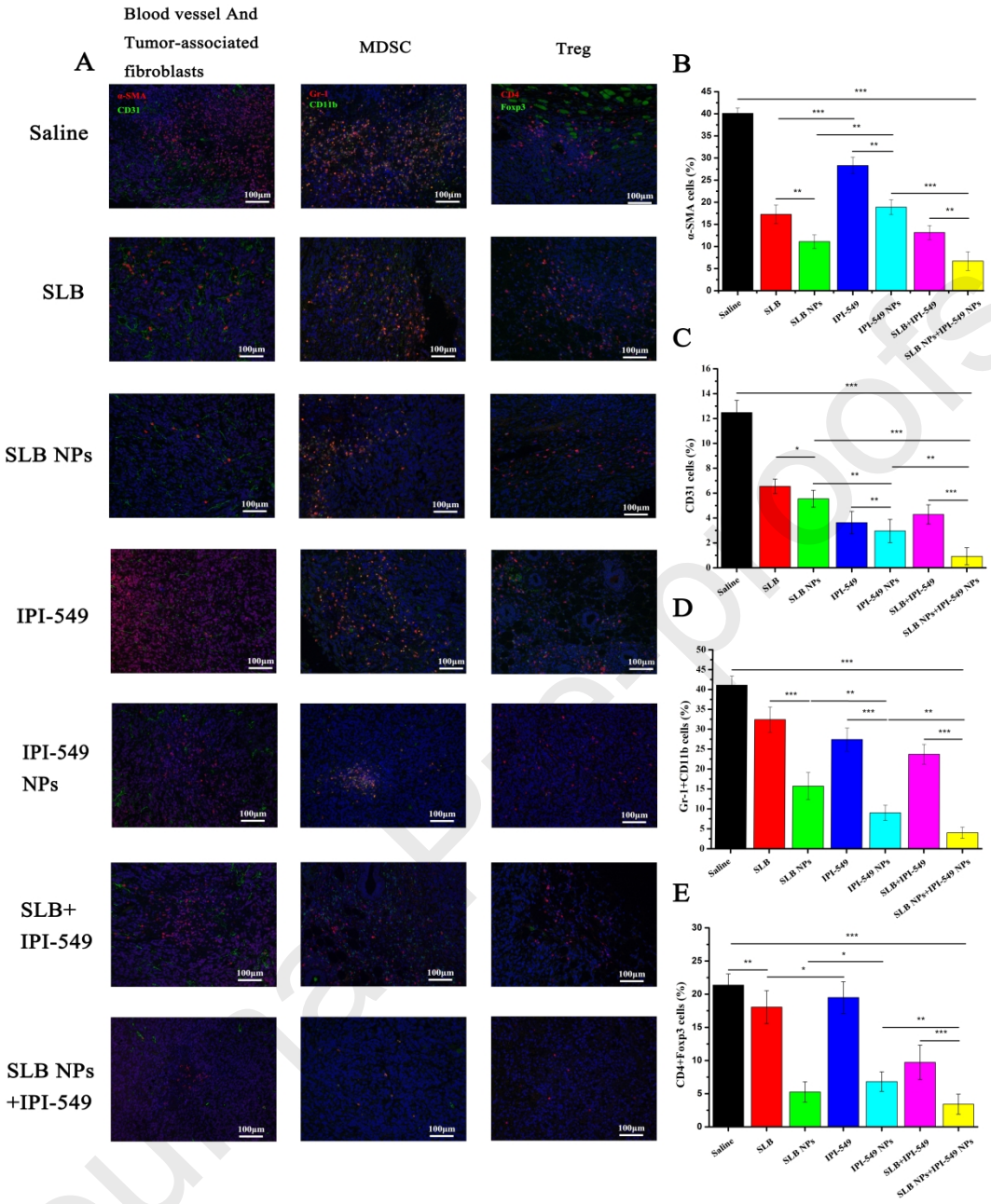
A
Blood vessel And Tumor-associated fibroblasts
MDSC
Treg
α-SMA
CD31
Gr-1
CD11b
CD4
Foxp3
100μm
Saline
SLB
SLB NPs
IPI-549
IPI-549 NPs
SLB+ IPI-549
SLB NPs +IPI-549
B
α-SMA cells (%)
C
CD31 cells (%)
D
Gr-1+CD11b cells (%)
E
CD4+Foxp3 cells (%)
Saline
SLB
SLB NPs
IPI-549
IPI-549 NPs
SLB+IPI-549
SLB NPs+IPI-549 NPs

Fig. 10

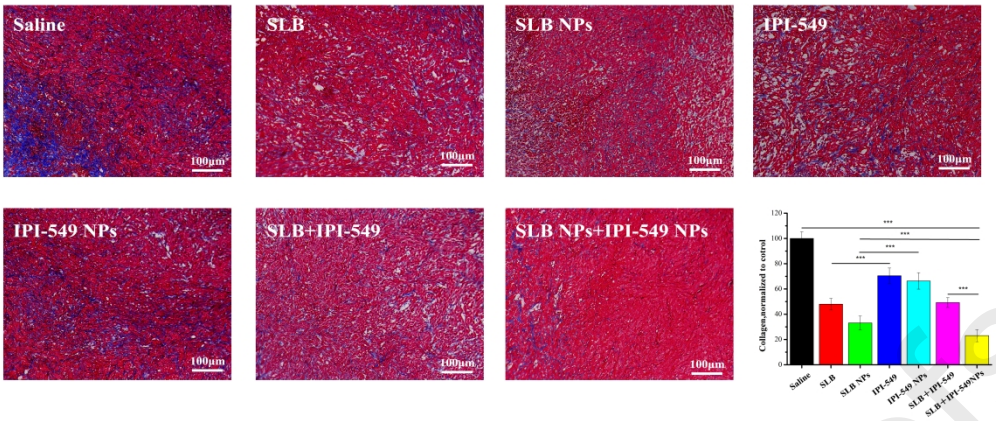

Fig. 11

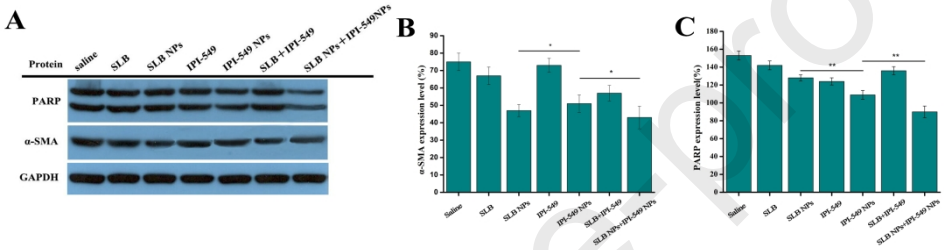

Fig. 12

Graphical abstract

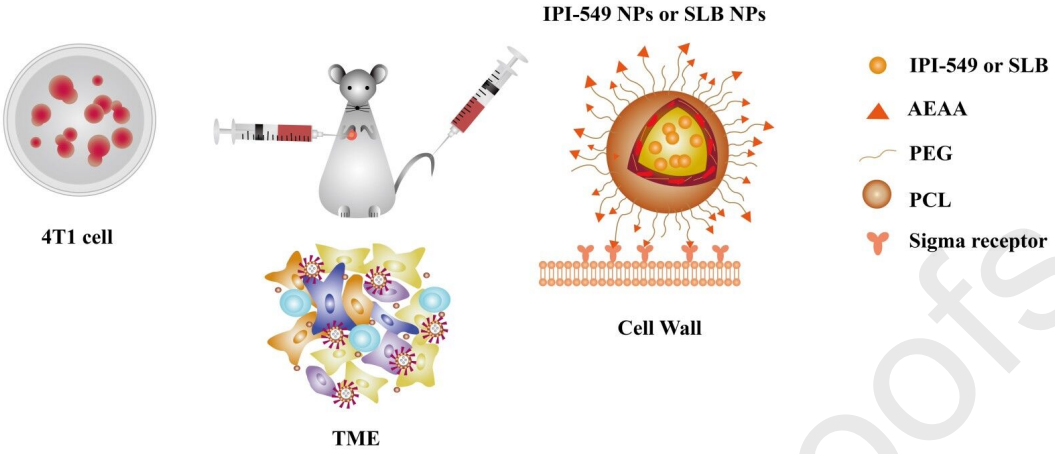

Credit Author Statement

All the authors listed have approved the manuscript that is enclosed. The manuscript has not been previously published, nor is currently considered for publication in any other journals.

Author contributions

Min Jiang: Conceptualization, Methodology, Software, Investigation, Writing - Original Draft.

Kaiyong He: Validation, Formal analysis, Visualization, Software.

QiuTong: Validation, Formal analysis, Visualization.

Jiahui Sun: Resources, Writing - Review & Editing, Supervision, Data Curation.

Qi Liu: Writing - Review & Editing, Supervision, Data Curation.

Xueqiong Zhang: Writing: Review & Editing.

Hua Zheng: Writing: Review & Editing.

Conflict of interest

The authors declare that they have no conflicts of interest.